NJC

ROYAL SOCIETY OF CHEMISTRY

PAPER

View Article Online
View Journal

Cite this: DOI: 10.1039/d1nj02368c

Pesticide degradation on solid surfaces: a moisture dependent process governed by the interaction between TiO_2 and H_2O†

Wenda Yang,‡[a] Zhongwen Wang,‡[a] Bin Yang,[a] Yu Jiang,[a] Meizhou Sun,[a] Xinghuan Liu,[a] Babar Amin,[a] Guixian Ge,[b] Raul D. Rodriguez*[c] and Xin Jia*[a]

Received 13th May 2021,
Accepted 4th June 2021

DOI: 10.1039/d1nj02368c

rsc.li/njc

Photocatalysis with universality and feasibility has been widely applied to degrade pollutants that mainly exist in gas and liquid systems. However, the photocatalytic degradation of contaminants on solid surfaces is rarely reported. The investigation of the photocatalytic degradation mechanism of pesticide on a solid surface will provide a vital reference for removing pesticide residues on fruit surfaces. Here, we discovered that *in situ* photocatalytic degradation on solid surface (PDSS) is a moisture dependent process regulated by the interaction between TiO_2 and H_2O. The interaction mechanism between TiO_2 and moisture was revealed by X-ray photoelectron spectroscopy and *in situ* FT-IR. Meanwhile, we investigated a water layer formed between TiO_2 and water on the surface by density functional theory. The photocatalytic degradation process of imidacloprid on the solid surface is proposed. This work explores the H_2O impact on photocatalysis in solid surfaces and provides a significant reference for removing pesticide residues in realistic environmental conditions.

1. Introduction

Pesticide residues are widespread and highly prevalent, especially on the surface of fruits and vegetables, which could cause plenty of dominant-negative effects,[1–5] such as chronic diseases and cancer.[6–8] Hence, removing pesticide residues using convenient methods is a crucial challenge that affects agriculture, health, and food safety. At present, several ways have been reported, for instance, physical[9] (peeling, abluent[10] and ultrasound,[11] chemical[12,13] (ozonation[14,15])), and biological[16,17] (biological enzymatic hydrolysis[18]) methods. However, these methods fail to completely reduce pesticide residue levels, waste resources, and give rise to re-pollution. Hence, we are obliged to seek a more advantageous way to degrade pesticide residues.

Photocatalysis is applied in various fields because it is a pro-environment, sustainable and pollution-free technology.[19–22] Typical applications of photocatalysis include degradation of dye,[23–25] poisonous gas[26–29] and pesticide residues,[30–33] such as, degradation and monitoring of imidacloprid in industrial wastewater.[34] Photocatalytic degradation of imidacloprid by composite catalysts $H_3PW_{12}O_{40}$/La-TiO_2.[35] Pesticide degradation is carried out in aqueous solution or in the gas phase. However, it is obvious that PDSS is more appropriate for practical applications than in aqueous solutions because of its versatility and simplicity, such as self-cleaning[36–38] the solid phase degradation of polystyrene[39] and polyvinyl chloride.[40] Therefore, we consider it to be feasible to degrade pesticide residues on solid surfaces. Previous studies showed that environmental conditions (humidity and temperature) are critical to the processes behind photocatalytic degradation.[41,42] For example, in the photocatalytic gas-solid systems, relative humidity (RH) was shown to play a significant role in VOC degradation.[43] Similarly, we believe that RH is also essential for solid-phase degradation. Exposing the influence of moisture on *in situ* photocatalytic degradation on the solid-phase is beneficial to the efficient removal of pesticide residues. There have been numerous studies on the interaction between TiO_2 and water.[44–46] The interfacial structure between H_2O and TiO_2 was explored, which was comprised of H_2O molecules and an ordered array of hydroxyls in the second layer.[47] The surface structure of TiO_2 was determined by the adsorbed water

[a] School of Chemistry and Chemical Engineering/Key Laboratory for Green Processing of Chemical Engineering of Xinjiang Bingtuan, Key Laboratory of Materials-Oriented Chemical Engineering of Xinjiang Uygur Autonomous Region, Engineering Research Center of Materials-Oriented Chemical Engineering of Xinjiang Bingtuan, Shihezi University, Shihezi 832003, People's Republic of China. E-mail: jiaxin@shzu.edu.cn

[b] Shihezi University Shihezi Univ, Coll Sci, Dept Phys, Shihezi 832003, People's Republic of China

[c] Tomsk Polytechnic University, 30 Lenin Avenue, 634050 Tomsk, Russia. E-mail: raul@tpu.ru

† Electronic supplementary information (ESI) available. See DOI: 10.1039/d1nj02368c

‡ These authors contributed equally to this work.

molecules.[44,48,49] H_2O enhanced electrons and holes trapping dynamics on the anatase TiO_2 surface, which were largely affected by the nanostructure spatial confinement.[50,51] Most recently, the isolated terminal hydroxyl (OH_T) and bridged hydroxyl groups (OH_B) on the surface of TiO_2 were used as Brønsted acid/base sites for moisture.[52,53] The first water molecule layer at the $TiO_2(001)/H_2O$ interface was important for its dynamic structure.[54] An unprecedented long-range ordered H_2O monolayer on $TiO_2(101)$ anatase was directly observed by scanning tunneling microscopy.[55] The interaction of TiO_2 and moisture determines the degradation mechanism of *in situ* photocatalysis on the solid-phase surface. Whereas the mechanism, feasibility, and effect of water on surface degradation were rarely revealed.

Based on the previous reports discussed above, here, we study the humidity-controlled photocatalytic degradation of pollutants to reveal the working mechanism on solid surfaces. We demonstrate the absorbed water on the TiO_2 surface *via* IR and dynamic water adsorption experiments (DVS). The hydrogen bond between TiO_2 and moisture enhanced the photo-generated charge carrier separation efficiency, which was characterized by *in situ* IR and photoelectrochemical measurements. We evaluated the degree of surface hydroxylation by XPS. DFT results showed the structure of a water layer on the TiO_2 surface and its effect on oxygen. We found that the adsorption of water increases the transfer distance of charge and the formation of water layer on the surface of TiO_2 prevents oxygen from participating in the reaction, which reduces the charge separation efficiency and affects the photodegradation of pollutants. The photocatalytic degradation intermediates of imidacloprid were identified *in situ* by LC-MS. Based on these collective experimental and calculation results, we propose a possible degradation pathway that takes environmental effects into account. This work shows new insights on the influence of moisture and TiO_2 interaction to the *in situ* photocatalytic degradation of pesticide residues on the solid-phase surface.

2. Experimental

2.1 Materials

Commercial TiO_2 (Degussa P25 grade, 20% rutile and 80% anatase) was obtained from Acros organics (Japan). Imidacloprid (IMD, >99.0% purity) was obtained from Yuanye Bio-Technology (Shanghai). Acetonitrile (HPLC grade) was obtained from Thermo Fisher Scientific (America). Apples grown in the Xinjiang region were obtained from local markets.

2.2 Solid-phase photocatalytic degradation of imidacloprid on glass/apple surface

2.2.1 Photocatalytic degradation of IMD on glass surface. Firstly, an ethanol solution of IMD and TiO_2 with a certain concentration was prepared. 400 μL IMD solutions were evenly coated on 4 × 2 cm glass pieces used as supports and were dried in an oven at 50 °C for 10 h. Then the different amounts of TiO_2 (2–6 mg) were deposited on the IMD-coated glass sheet. A sun simulated illumination (400 mW cm^{-2}) served as the light source. After 1–4 h light irradiation, the glass slices were immersed in 10 mL ethanol and ultrasonicated for 1 h, so that the residual IMD was completely dissolved in ethanol and monitored by an ultraviolet spectrophotometer.

2.2.2 Photocatalytic degradation of IMD on apple surfaces. We use apples as the research basis for simulation experiments, and the specific process is as follows: First of all, the pesticide residue on the apple surface was removed by ultrasonic cleaning. Then the apples were soaked in the 50.00 mg L^{-1} IMD solution for 24 h, and a uniform solution of TiO_2 was sprayed on the surface. Finally, the apple substrate samples obtained were placed in a temperature and humidity control system (T 20–40 °C, RH 20–90%), using the light source shown in Fig. 1. The specific testing process is as follows:

Extraction. A 10.00 g apple peel sample was placed in a 100.00 mL centrifuge tube, 20.00 mL acetonitrile was added and IMD was extracted by 15 000 rpm centrifugation for 5 min. 10 mL supernatant was extracted and added to a 50 mL pear-shaped bottle, rotary steamed at 38 °C to near dryness, and then 25% acetonitrile was added to the pear-shaped bottle. The sample was ultrasonicated for 30 seconds to fully dissolve and wait for purification.

Purification. First, the ENVI-18 column is pre-eluted with 5 mL acetonitrile, then the column is equilibrated with 5 mL 25% acetonitrile, and then 1 mL of the dissolved sample extract is transferred from the pear-shaped bottle to the purification column. Then the column was rinsed with 10 mL of 20 mmol L^{-1} NaOH solution and 10 mL of water, and the column was drained. Finally, the imidacloprid retained on the column was slowly eluted with 2 mL of acetonitrile, and filtered with a 0.45 μm organic filter membrane for testing.

Detection. (a) Column: C18 (5 μm, 250 mm × 4.6 mm)
(b) Injection volume: 5 mL; Wavelength: 270 nm
(c) Result calculation
The residual amount of imidacloprid is calculated according to formula (1):

$$X = \frac{A_1 \times V_1 \times V_3 \times c}{A_2 \times V_2 \times m} \quad (1)$$

where: X is the content of pesticides in the sample (mg Kg^{-1}); A_1 is the peak area of the components in the sample; V_1 is the total volume extracted from the sample (mL); V_3 is the volume

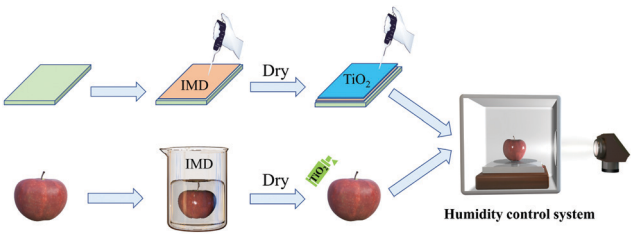

Fig. 1 Photocatalytic degradation system for IMD on the solid phase surface.

after purification (mL); c is the standard mass concentration (mg L^{-1}); A_2 is the peak area of the components in the standard sample; V_2 is the total volume of the extraction solution for purification (mL); m is the mass of the sample (kg).

2.3 Photoelectrochemical measurements

The pre-treated TiO_2 was coated on the ITO substrate as an integrated photoelectrode, and the photocurrent and electrochemical impedance were recorded in a standard three-electrode system. Firstly, the ITO electrodes were ultrasonically cleaned in deionized water, acetone, and ethanol in sequence.[56] Then 1 mg of the catalyst was dissolved in 1 mL of ethanol solution (water : ethanol = 1 : 2), and 20 μL of the mixture was coated on half of the 1 × 2 cm ITO electrode and inserted into the quartz with 0.20 M Na_2SO_4 aqueous solution as the electrolyte in the container. The saturated Ag/AgCl electrode, a Pt plate and the catalyst deposited on an ITO substrate were used as the reference electrode, counter electrode and working electrode, respectively.[57] Under the irradiation of a 400 MW cm^{-2} xenon lamp, the electrochemical impedance spectroscopy (EIS) of the catalyst was recorded. Under an applied potential of −0.4 V, the transient photocurrent response was detected. All samples were subjected to light treatment at different humidity before testing.

2.4 Characterization

Optical transmittance spectra of the degradation of IMD were recorded using a UV-Vis spectrophotometer (MAPADA, Shanghai). Dynamic water adsorption experiments were performed characterized using an Advantage Instrument (UK) at different relative humidity. The infrared spectra were monitored using a FTIR spectrometer (Bruker Vertex 70 V). To measure the mineralization efficiency, a TOC-VCPH analyzer was used to analyze the total organic carbon (TOC) of the degraded IMD (TC is completely burned at 850 °C, TIC was treated by phosphorylation, and Pt was used as the catalyst). X-ray photoelectron spectroscopy (XPS) was recorded on an Escalab Xi+ (Thermo Fisher Scientific, US).

2.5 *In situ* infrared spectroscopy test

Humidity *in situ* infrared spectroscopy was performed using an IR spectrophotometer (Nicolet Nexus 670) equipped with a humidity and temperature control system (Fig. 2). The side of the *in situ* infrared sample cell is composed of a glass tube that can pass ultraviolet light, a CaF_2 window piece and an injection port sealed at both ends for infrared testing. A 250 nm main wavelength lamp is installed above the infrared pool as the light source. The catalyst is filled in the sample rack in the sample tank. The sample rack is made of Teflon material. The DTGS KBR detector was adopted with a scanning band of 4000–500 cm^{-1}, 32 scanning runs and a resolution of 4 cm^{-1}. The changes of transmission spectra were recorded by an *in situ* infrared spectrometer. Samples were completely dried before the spectra were recorded.

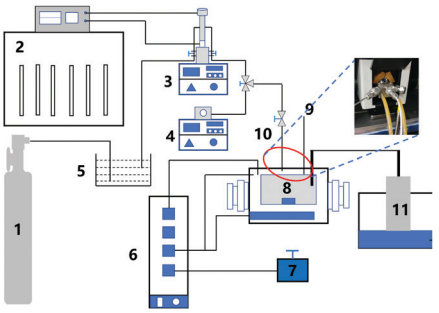

Fig. 2 1. N_2 cylinder, 2. Cooling pump, 3. High pressure injection pump, 4. Metering pump, 5. Humidifier, 6. Controller, 7. Magnetic stirring, 8. Sample pool, 9. Exhaust valve, 10. Intake valve, 11. FT-IR spectrometer, 12. The computer.

2.6 Intermediate analysis

IMD and intermediate products were separated by SB-C18 RRHD (Agilent, 2.1 × 100 mm, 1.8 μm). Both the standard sample and the reaction mixture were separated by a mobile phase consisting of 0.20% formic acid solution (solvent A) and acetonitrile (solvent B) under the same volume. 85, 80, 75, 0, and 85% of solvent A were added and solvent B was added to the rest at 0, 3, 22, 23, and 29 min, respectively. The flow rate of the mobile phase was 0.40 mL min^{-1}, the total injection volume was 5.00 μL, and the temperature was kept at 25 °C. The total running time was about 30 min. The ESI interface operated in positive ion mode, and the voltage was set to 80 V. A full-spectrum scan from 65 to 500 m/z was recorded at a scan rate of 500 amu s^{-1}.

3. Results and discussion

3.1 Effect of RH on photocatalytic solid phase degradation

We show in Fig. 3 the moisture dependence of the degradation efficiency of IMD within the range 20–90% RH. The IMD residues after degradation for 1 h are in the order of 43%, 36%, 28%, 23%, 26% and 30% with RH in the order of 20%, 40%, 60%, 70%, 80% and 90%. The degradation at 70% RH is slightly higher than the other RH because of the different moisture adsorbed on the surface of TiO_2. The water molecules

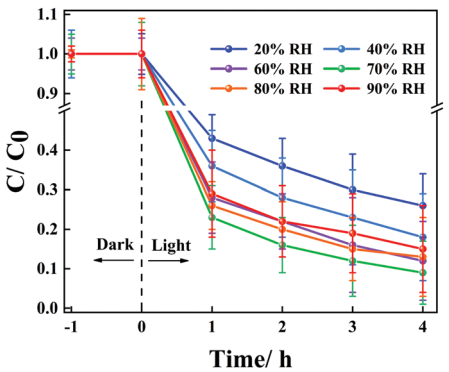

Fig. 3 Effects of RH on *in situ* photocatalytic degradation of IMD on the solid surface.

on the surface of TiO_2 will affect the efficiency of electron transport, and thus the degradation decreases too. Nevertheless, the degradation performance of TiO_2 towards IMD is still relatively good and the pesticide can be fully degraded at high RH. We performed IMD degradation experiments with TiO_2 under different illumination times. The efficiency for degradation of IMD under photocatalytic conditions were 91% after 4 h, which is comparable to that of the liquid system, *i.e.*, 30.00 mg TiO_2 dispersed in 50.00 mL (10 mg L^{-1}) IMD solution, and the degradation efficiency was 91% (after 50 min). However, increasing the illumination time did not further increase the rate of IMD degradation. We believe that the contact between IMD and TiO_2 will not change in the solid-phase, IMD in direct contact with TiO_2 will be rapidly degraded by the TiO_2 hydroxyl vapor radicals under illumination.

Fig. S1(a) (ESI†) shows how the IMD degradation efficiency depends on TiO_2 quality. The degradation efficiency was 77% after 1 h for an optimal catalyst dose of 4.00 mg. However, increasing the amount of TiO_2 further decreased the degradation efficiency because of excess TiO_2 blocking photon transmission. Temperature also plays a role in *in situ* photocatalytic solid-phase degradation of IMD. Fig. S1(b) (ESI†) shows a comparison of IMD degradation by TiO_2 at different temperatures. The temperature increase promotes the degradation efficiency. However, for practical field applications, the temperature is limited by the actual environment.

3.2 Characteristics of the interaction between TiO_2 and H_2O

Photocatalytic degradation of IMD on solid-phase surfaces requires active oxygen species (h^+, $^\bullet OH$, O_2^-). To investigate the PDPSS in detail, we added different scavengers to the *in situ* photodegradation system to carry out free radical and hole trapping experiments. Isopropyl alcohol (IPA), triethanolamine (TEOA) and benzoquinone (BQ) were used to quench hydroxyl radicals ($^\bullet OH$), holes (h^+) and superoxide radicals (O_2^-), respectively. We see from Fig. 4(a) that when IPA was added, the photocatalytic reaction is severely inhibited, indicating that OH is the most significant active radical. The addition of TEOA and BQ also has a certain effect on the photocatalytic performance, showing that h^+ and O_2^- also take part in the photocatalytic reaction,[58] although playing a secondary role. RH is crucial for the photocatalytic reaction on solid surfaces, and since the surface of TiO_2 is hydrophilic, the moisture adsorption is humidity dependent. Fig. 4(b) shows that the surface adsorption capacity of TiO_2 increases with the increase of humidity. At 20–70% RH, the amount of moisture adsorbed on the TiO_2 surface shows an upward trend, but it has little change. The adsorption capacity of TiO_2 to moisture augments sharply at 70–90% RH. With the adsorption increase, it is possible to form a water layer physisorbed on the TiO_2 surface, isolating TiO_2 from the external environment, and explaining to a certain extent the phenomenon we observed at the beginning. FT-IR spectroscopy was used to verify the existence of water molecules on the TiO_2 surface during the reaction process.

As shown in Fig. 4(c), after reacting at different RH, several peaks appeared in the spectrum at higher RH environments as compared with that at low RH. Peaks at 3426 and 1632 cm^{-1} are ascribed to the stretching vibration and bending vibration of OH, while those at 651 cm^{-1} could be assigned to the characteristic absorption peak of TiO_2. No absorption peak corresponding to OH is visible for experiments at RH of 20–40%, indicating that water failed to adsorb on the TiO_2 surface. When humidity increases further, the appearance of OH is observed. Infrared spectroscopy shows that water exists on the surface of TiO_2 at high humidity. Before the FTIR experiments, the TiO_2 was vacuum dried for 24 h.

We observed a significantly different profile in the *in situ* IR spectra from the water adsorbed on TiO_2. Results in Fig. 5(a) shows that at 3650–3000 cm^{-1} and 1500–1700 cm^{-1} vibrations from H_2O increase, including OH stretching $\nu(H_2O)$ and bending vibrations $\delta(H_2O)$, respectively. In the meantime, two extraordinary reversal peaks at 3728 and 3665 cm^{-1} appeared. These two peaks are equal to the ν(OH) vibration of the isolated

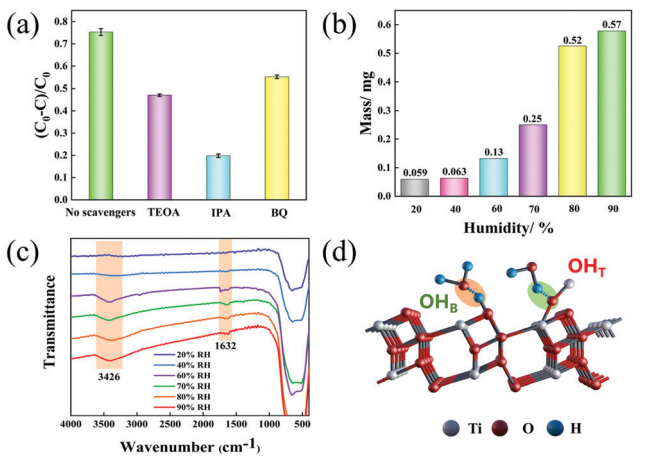

Fig. 4 Free radical capture experiment (a); dynamic water adsorption experiment (DVS) (b); FT-IR spectra (c); model of the interaction between TiO_2 and water (d).

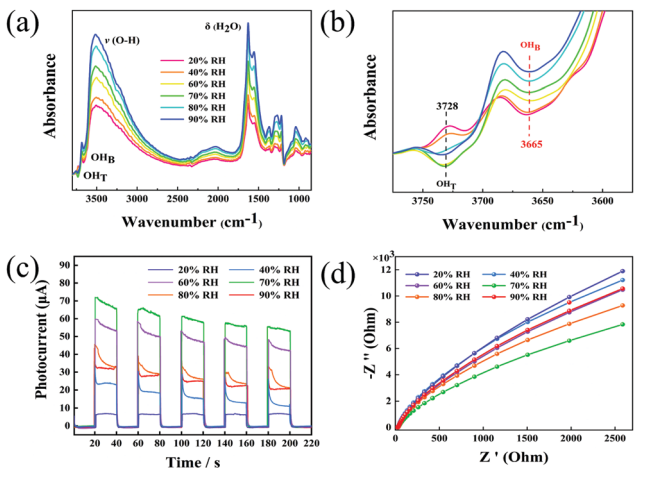

Fig. 5 *In situ* IR spectra: as the humidity increases (a); enlarged scales of the ν(OH) of the isolated surface OH_B and OH_T (b); transient photocurrent responses (c) and EIS (d).

terminal hydroxyl (OH_T) and bridged hydroxyl groups (OH_B).[50,59] We clearly see that the presence of OH_T and OH_B at these positions decreases with the increase of RH. Fig. 5(b) shows that the introduction of water molecules at the beginning causes the reduction of OH_T and OH_B, but this change is not monotonic. On the surface of TiO_2, OH_B and OH_T are used as acid/base adsorption sites to further adsorb water molecules through intermolecular hydrogen bonds (Fig. 4(d)).

We conducted a photocurrent measurement on TiO_2 with different hydroxyl concentrations on the surface treated by light under different RH. The results show (Fig. 5(c)) that the higher the surface hydroxyl concentration of TiO_2, the stronger the photocurrent response and the higher the separation efficiency of photogenerated charges. This supports the excellent performance of photocatalytic degradation of IMD on solid surfaces. This is consistent with the experimental conclusion of Fu *et al.*[60] This experiment shows that light treatment under different RH can make the surface of TiO_2 have different concentrations of hydroxyl groups, and the higher the RH, the higher the surface hydroxyl concentration, the stronger the photocurrent response signal, and the higher the separation efficiency of photogenerated charges. When the RH exceeds 70%, the surface hydroxyl concentration decreases and the photocurrent intensity decreases, which inhibits the effective separation of photo-generated charges, which is not conducive to photocatalytic degradation of IMD on solid surfaces. This is also consistent with our results of TiO_2 photocatalytic degradation of IMD on the solid surface under different RH. We show the resulting recombination resistance at different humidity in the Nyquist plot in Fig. 5(d). The relative dimensions of the semicircle correspond to the charge separation efficiency and transfer resistance of photogenerated electron–hole pairs. The interface impedance of TiO_2 at 70% RH (T-70) is smaller than that of other samples. We believe that it facilitates electron transfer by forming hydrogen bonds between TiO_2 and H_2O, which can enhance the electron hole separation and the interface charge transfer.

The XPS survey spectra of TiO_2 and T-70 in Fig. 6 shows that these two materials matched exactly. It shows the existence of elemental Ti, O, and C, with Ti2p as the main component in the spectra with the highest intensity, the narrowest peak width, and the highest symmetry. In addition to the main spectral line Ti2p, there were other spectral lines such as Ti2s, Ti3s, and

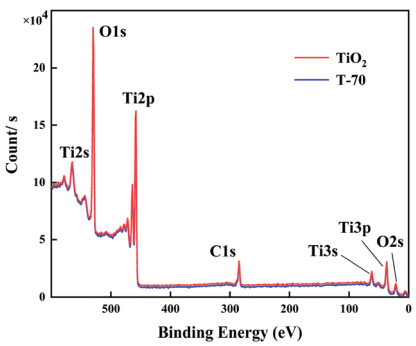

Fig. 6 XPS survey scan of TiO_2 and T-70.

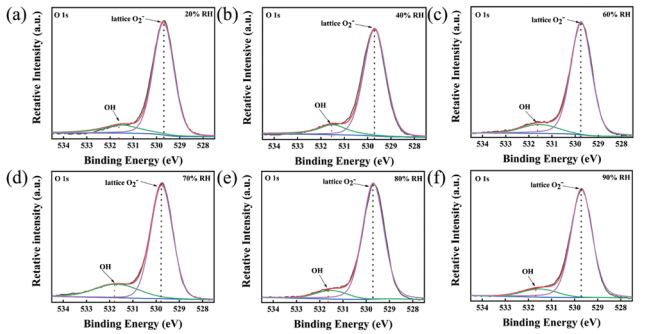

Fig. 7 XPS spectra of TiO_2 at 20% (a), 40% (b), 60% (c), 70% (d), 80% (e) and 90% RH (f).

Ti3p. XPS was used to characterize the OH oxidation state. The coexistence of OH and lattice O_2^- in the TiO_2 catalyst was evidenced by a shoulder observed on the peak at 529.7 eV and 532.5 eV, that evidenced the presence of molecules in TiO_2. The degree of surface hydroxylation increased with increasing humidity in the range 20–70% RH (Fig. 7(a–d)). At higher RH 70–90%, the XPS results in Fig. 7(e and f) show that hydroxylation decreased, with lower content of hydroxyl group OH_T and OH_B that acts as an adsorption site for water. The OH percentages in TiO_2 confirmed by XPS are shown in Table 1. At 20–70% RH, O_2 and H_2O compete for adsorption on the surface of TiO_2, and O_2 is dominant, but trace amounts of OH can be found. At 70% RH, a water layer is formed on the surface of TiO_2, and lots of OH is generated by water molecules. At 70–90% RH, the generated OH further adsorbs H_2O, so a small amount of OH will be detected. The degree of hydroxylation was the largest on the surface of T-70, that also showed the best catalytic performance.

3.3 Density functional theory (DFT) calculations

We performed *ab initio* molecular dynamics (AIMD) calculations to clarify the effect of RH on the adsorption behaviour of H_2O. To reveal the effect of humidity in this calculation, we used models containing different proportions of H_2O and O_2 implemented in the Vienna Ab initio Simulation Package (VASP).[61,62] The $TiO_2(101)/H_2O$ and O_2 interfaces were modeled by a periodic supercell. Each supercell was composed of an anatase (101)-2 × 4 slab consisting of four O–Ti–O layers (about 6 Å) in contact with a mixing environment of H_2O and O_2 filling in the space between consecutive slabs. The optimized geometric parameter of thte $TiO_2(101)$ slab is a = 11.084Å and

Table 1 The OH percentage content in TiO_2 at different RH

	Peak position	
RH/%	Lattice O_2^- (532.5 eV)/%	OH (529.7 eV)/%
20	94.32	5.68
40	93.35	6.65
60	92.99	7.01
70	78.3	21.7
80	93.9	6.1
90	94.71	5.29

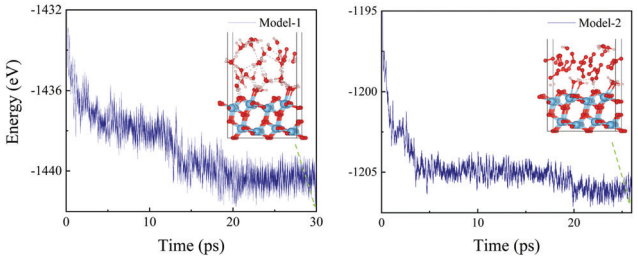

Fig. 8 Snapshot of a water layer on the TiO_2 interface obtained from AIMD simulations. Ti5c atoms are depicted in light blue, O is shown red and H is shown in light pink. The dashed lines represent hydrogen bonds.

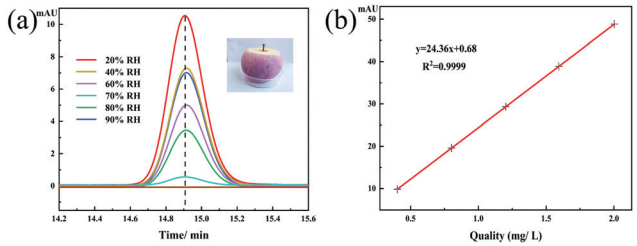

Fig. 9 The peak area of IMD residues at 20%, 40%, 60%, 70%, 80%, and 90% RH (a); the linear relationship between the quality and peak area (b).

b = 14.926 Å. One of the models involves $37H_2O$ and $3O_2$ molecules to simulate the case of higher RH. To simulate the lower RH, another model included only $10H_2O$ and $20O_2$ molecules. The canonical *NVT* ensemble was used with a Nose–Hoover thermostat[63] at T = 300 K. Each time step is set to 1 fs, and simulations were conducted for more than 25 000 steps (25 ps) which is long enough to obtain reliable structural information. In addition, the DFT-D3 dispersion correction proposed by Grimme[64] was utilized to provide a better description of long-range van der Waals (vdW) interactions.

Snapshots from the AIMD simulations of the two models are shown in Fig. 8. For the two models, the H_2O molecules adsorbed on the TiO_2(101) surface to form a stable configuration after about 20 ps. In Model-1, all of the Ti5c sites are occupied by one H_2O molecule, and the rest of the H_2O molecules made a water overlayer through H-bonding interactions. Thus, the charge separation efficiency and photocatalytic performance were suppressed because of the obstruction of the H_2O overlayer that blocked the induced dissociative O_2 molecule from taking part in the photocatalytic reaction. This situation directly compromises the *in situ* degradation of pesticide residues. In contrast, the result for lower RH, we found that the Ti5c sites in Model-2 are partially occupied by the H_2O molecules and no H_2O overlayer is formed. The dissociative O_2 molecule would approach the TiO_2(101) surface and be reduced by the photo-generate electrons promoting the photocatalytic reaction forward.

3.4 Degradation of IMD on apple surfaces

The apple as a research substrate has important practical significance. The photocatalytic degradation of IMD on the apple surface was investigated by HPLC. Fig. 9(a) is a plot of the IMD remaining peak area *versus* time at different RH. The plot combined with the relationship between the quality and peak area (Fig. 9(b)) represent the IMD degradation efficiency. According to Table 2, we found that the influence of RH on the *in situ* IMD photocatalytic degradation on an apple surface was the same as on glass. We determined that 97.66% of IMD residues were removed from the apple surface at 70% RH. This degradation efficiency is better than the efficiency obtained on the glass substrate. We attribute the superior degradation performance on the apple to the apple's own moisture. The IMD residue (0.329 mg kg^{-1}) is within the US maximum residue limit (MRL) of 0.5 mg kg^{-1} for residual food pesticides. We further verified this result in the actual environment.

Table 2 The degradation efficiency of IMD on the apple's surface at different RH

	Area (mAU × S)	IMD (mg L^{-1})	Degradation rate/%
20% RH	131.59	5.34	51.97
40% RH	102.66	4.18	62.42
60% RH	73.02	2.96	73.38
70% RH	7.02	0.26	97.66
80% RH	50.68	2.05	80.04
90% RH	104.70	4.27	61.60

For demonstrations in practical applications, it is necessary to perform this photocatalytic experiment under natural conditions. IMD on the apples surface was degraded by outdoor sunlight (T 30 ± 3 °C, RH 27 ± 5%). The degradation efficiency of IMD at different times in outdoor conditions is shown Fig. S1(c) (ESI†). IMD gets oxidized by reactive oxygen species generated by TiO_2 under ultraviolet light (UV) excitation. As there is only a small proportion of UV in natural light, adequate light is required to achieve the desired degradation efficiency. As a result, the degradation efficiency of IMD increases with the increase in exposure time. The degradation efficiency reaches values of up to 88% when the illumination time is 50 h. This degradation efficiency complies with MRLs in food. This experiment was in line with actual production scenarios and offered the necessary technological assistance for realistic applications. We notice that the extension of this experiment to real life conditions would be influenced by climate and other unpredictable factors.

3.5 Intermediates analysis

We evaluated the total content of organic carbon (TOC) from *in situ* photocatalytic solid-phase degradation of residual IMD. The mineralization efficiency presented in Fig. S1(d) (ESI†) shows the effect of humidity on TOC. The mineralization of organic matter is inhibited at lower or higher humidity. We found a 96% mineralization efficiency at 70% RH. The IMD was almost entirely mineralized into H_2O, CO_2 and inorganic substances. As we expected, this process has greater advantages over the solution reaction including high mineralization efficiency, less residual harmful substances, and lower secondary environmental pollution.

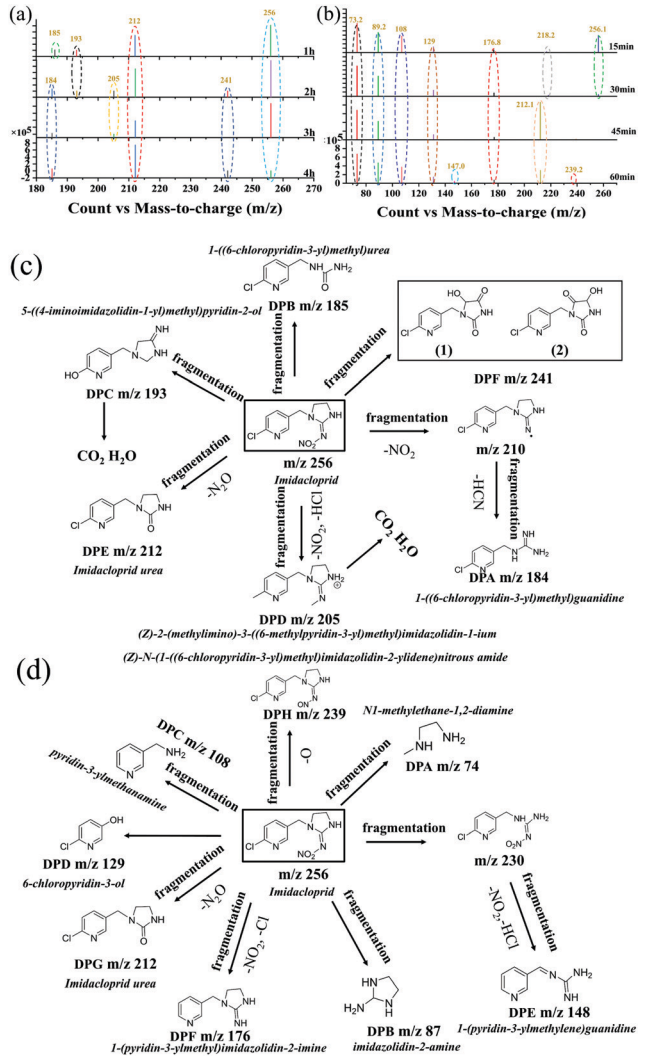

Fig. 10 Mass spectra and degradation pathways of IMD on the solid surface (a and c) and in the liquid phase (b and d).

Several products formed IMD decomposition, several products were formed. To explore possible pathways of degradation, LC-MS was performed to analyze the degradation products of IMD at 70% RH (Fig. 10(a)). According to the results from this experiment and from previous reports,[65,66] the possible routes for solid surface degradation of IMD are shown in Fig. 10(c). Above all, IMD (*m*/*z* 256) can be directly converted into the degradation product A (DPA, *m*/*z* 184) and DPD (*m*/*z* 205) by being attacked and losing $-NO_2$, –HCN and $-NO_2$, –HCl. Meanwhile, the fragmentation and hydroxylation of the parent compound formed DPB (*m*/*z* 185) and DPC (*m*/*z* 193), respectively. IMD got fragmented, lost $-N_2O$ and transformed into the most familiar IMD urea (*m*/*z* 212).[67,68] It is evident that there is a significant accumulation of products with the increase of illumination time. In particular, IMD leads to the formation of DPF (*m*/*z* 241), which has two isomers, including product (1) and (2). Two of them, DPC and DPD, are eventually converted to CO_2, H_2O, and inorganic substances. The products formed by photocatalytic degradation of IMD on the solid surface are more isolated than those in the liquid phase (Fig. 10(b) and (d)),[69] because the contact between IMD and TiO_2 is fixed and there is no solvent as the medium. The intermediate products will not contact each other and secondary reactions will occur avoiding the formation of additional intermediate products. Among them, the toxicity of some products is unknown and whether they pose a threat to human health. In this context, understanding the reaction pathway and the degradation mechanism is the best way to avoid unintended consequences arising.

3.6 Mechanism

We explain the observed experimental phenomena by analyzing the photocatalytic degradation mechanism of IMD on the solid surface. In the 20–70% RH range, H_2O and O_2 in the environment are adsorbed on the surface of TiO_2 by intermolecular hydrogen bonds to form active species ($^{\bullet}OH$, O_2^{-})[70,71] under the influence of light that degrades IMD (Scheme 1).

Hydrolytic adsorption in the air at 70% RH formed two classes of hydroxyl and occurs in the form of an adsorbed state on the solid surface. One is when water dissociates at ($O_{b\text{-}vac}$) to form bridged hydroxyl groups (OH_B) and the other one is when O in H_2O binds to the Ti5c surface to form an isolated terminal (OH_T). The TiO_2 surface is saturated with water molecules through hydrogen bonding between these two molecules, with the largest number of hydroxyl radicals generated. The bonding between molecules was conducive to the transmission of electrons, which suppresses the efficiency of electron–hole recombination efficiency and improved photocatalytic performance.[60] At 70–90% RH, H_2O got the absolute advantage over O_2 in the

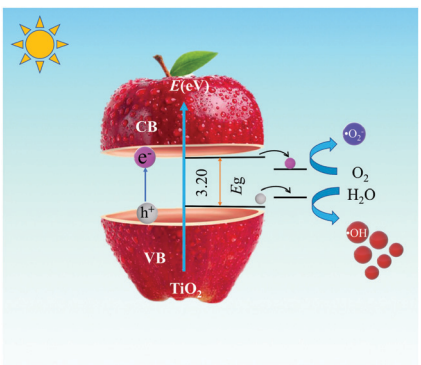

Scheme 1 Degradation of IMD on the TiO_2 surface.

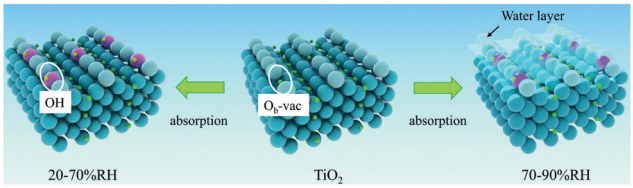

Scheme 2 A schematic diagram of the interaction between moisture and TiO_2. Ti5c is shown in light green, O in blue, Ob in light blue, adsorbed O in pink, and H is shown in yellow.

competitive adsorption process on TiO_2. The water layer was formed to adsorb water molecules through OH_B and OH_T on the TiO_2 surface (Scheme 2),[72] which occupies the active site, inhibited electron transport, and prevented O_2 from participating in the degradation reaction. O_2 induced the band to bend upwards and formed negatively charged compounds on the surface of TiO_2 that act as charge traps for photogenerated electrons inhibiting electron hole recombination.

4. Conclusions

In summary, the investigation of the reaction process in humidity-controlled systems evidences the impact of moisture on *in situ* photocatalytic degradation of organic contaminant on the solid surfaces. Our results revealed the interfacial structure between H_2O and TiO_2, showing that in the 20–70% RH range, water molecules dissociate to form hydroxyl radicals ($^{\bullet}OH$). Hydrogen bonding between TiO_2 and water molecules acts as an electron transport channel promoting the charge separation efficiency. The IMD removal rate reached the highest value of 77% after 1 h of light exposure. For higher humidity in the 70–90% RH range, a water layer formed on the surface of TiO_2 *via* absorption. The water layer prevents oxygen, which acts as an electron trapping agent, from participating in the reaction. Photo-generated charge carrier separation efficiency and degradation performance are inhibited. The remaining content of IMD after *in situ* photocatalytic solid-phase degradation meets the standards of US MRLs. The intermediates are single and nearly completely mineralized, avoiding secondary pollution to the environment. This new overall technique opens opportunities for degradation of organic contaminants based on the concept of *in situ* photocatalysis on the solid-phase surface under realistic environmental conditions.

Conflicts of interest

There are no conflicts to declare.

Acknowledgements

This study was supported by the National Natural Science Foundation of China (U1703351, 52073179, 51663021), Bingtuan Excellent Young Scholars (CZ027205) and Bingtuan Science & Technology Nova Program. We wish to thank the Analysis and Testing Center of Shihezi University for the microscopy and microanalysis of our specimens. RDR thanks support by the Tomsk Polytechnic University 5-100 Program.

References

1 Z. A. Abd-Elhaleem, *Environ. Sci. Pollut. Res.*, 2020, **27**, 8526–8534.
2 C. J. Topping, A. Aldrich and P. Berny, *Science*, 2020, **367**, 360–363.
3 L. M. Bexfield, K. Belitz, B. D. Lindsey, P. L. Toccalino and L. H. Nowell, *Environ. Sci. Technol.*, 2021, **55**, 362–372.
4 D. H. Quinones, A. Rey, P. M. Alvarez, F. J. Beltran and G. L. Puma, *Appl. Catal., B*, 2015, **178**, 74–81.
5 H. Zhao, W. Hasi, N. Li, X. Sha, S. Lin and S. Han, *New J. Chem.*, 2019, **43**, 13075–13082.
6 A. Samsidar, S. Siddiquee and S. M. Shaarani, *Trends Food Sci. Technol.*, 2018, **71**, 188–201.
7 Y.-H. Chiu, H. Sandoval-Insausti, S. H. Ley, S. N. Bhupathiraju, R. Hauser, E. B. Rimm, J. E. Manson, Q. Sun and J. E. Chavarro, *Environ. Int.*, 2019, **132**, 105113.
8 F. L. Souza, C. Saez, M. R. V. Lanza, P. Canizares and M. A. Rodrigo, *Appl. Catal., B*, 2016, **180**, 733–739.
9 O. Kitous, A. Cheikh, H. Lounici, H. Grib, A. Pauss and N. Mameri, *J. Hazard. Mater.*, 2009, **161**, 1035–1039.
10 T. Yang, J. Doherty, B. Zhao, A. J. Kinchla, J. M. Clark and L. He, *J. Agric. Food Chem.*, 2017, **65**, 9744–9752.
11 S. M. R. Azam, H. Ma, B. Xu, S. Devi, M. A. B. Siddique, S. L. Stanley, B. Bhandari and J. Zhu, *Trends Food Sci. Technol.*, 2020, **97**, 417–432.
12 M. Tang, Y. Ao, C. Wang and P. Wang, *Appl. Catal., B*, 2020, **268**, 118395.
13 M. A. Kamboh, W. A. W. Ibrahim, H. R. Nodeh, M. M. Sanagi and S. T. H. Sherazi, *New J. Chem.*, 2016, **40**, 3130–3138.
14 D. H. Quiñones, A. Rey, P. M. Álvarez, F. J. Beltrán and G. Li Puma, *Appl. Catal., B*, 2015, **178**, 74–81.
15 R. Pandiselvam, R. Kaavya, Y. Jayanath, K. Veenuttranon, P. Lueprasitsakul, V. Divya, A. Kothakota and S. V. Ramesh, *Trends Food Sci. Technol.*, 2020, **97**, 38–54.
16 B. J. Mahler, T. S. Schmidt, L. H. Nowell, S. L. Qi, P. C. Van Metre, M. L. Hladik, D. M. Carlisle, M. D. Munn and J. May, *Environ. Sci. Technol.*, 2020, **54**, 5509–5519.
17 M. Nehra, N. Dilbaghi, G. Marrazza, A. Kaushik, C. Sonne, K.-H. Kim and S. Kumar, *J. Hazard. Mater.*, 2021, **401**, 123369.
18 A. Sharma, V. Kumar, R. Bhardwaj and A. K. Thukral, *Toxicol. Environ. Chem.*, 2016, **99**, 95–103.
19 L. Zeng, X. Guo, C. He and C. Duan, *ACS Catal.*, 2016, **6**, 7935–7947.
20 L. Noureen, Z. Xie, Y. Gao, M. Li, M. Hussain, K. Wang, L. Zhang and J. Zhu, *ACS Appl. Mater. Interfaces*, 2020, **12**, 6343–6350.
21 J. M. Herrmann, C. Duchamp, M. Karkmaz, B. T. Hoai, H. Lachheb, E. Puzenat and C. Guillard, *J. Hazard. Mater.*, 2007, **146**, 624–629.
22 Y. Yang, M. Wu, X. Zhu, H. Xu, S. Ma, Y. Zhi, H. Xia, X. Liu, J. Pan, J.-Y. Tang, S.-P. Chai, L. Palmisano, F. Parrino, J. Liu, J. Ma, Z.-L. Wang, L. Tan, Y.-F. Zhao, Y.-F. Song, P. Singh, P. Raizada, D. Jiang, D. Li, R. A. Geioushy, J. Ma, J. Zhang, S. Hu, R. Feng, G. Liu, M. Liu, Z. Li, M. Shao, N. Li, J. Peng, W.-J. Ong, N. Kornienko, Z. Xing, X. Fan and J. Ma, *Chin. Chem. Lett.*, 2019, **30**, 2065–2088.
23 Q. Li, T. Zhao, M. Li, W. Li, B. Yang, D. Qin, K. Lv, X. Wang, L. Wu, X. Wu and J. Sun, *Appl. Catal., B*, 2019, **249**, 1–8.
24 W. Hong, C. Li, T. Tang, H. Xu, Y. Yu, G. Liu, F. Wang, C. Lei and H. Zhu, *New J. Chem.*, 2021, **45**, 2631–2642.

25 Q. Sun, K. Li, S. Wu, B. Han, L. Sui and L. Dong, *New J. Chem.*, 2020, **44**, 1942–1952.
26 X. Zhu, C. Jin, X.-S. Li, J.-L. Liu, Z.-G. Sun, C. Shi, X. Li and A.-M. Zhu, *ACS Catal.*, 2017, **7**, 6514–6524.
27 N. Lv, Y. Li, Z. Huang, T. Li, S. Ye, D. D. Dionysiou and X. Song, *Appl. Catal., B*, 2019, **246**, 303–311.
28 Q. Huang, Y. Hu, Y. Pei, J. Zhang and M. Fu, *Appl. Catal., B*, 2019, **259**, 118106.
29 B. Hauchecorne, T. Tytgat, S. W. Verbruggen, D. Hauchecorne, D. Terrens, M. Smits, K. Vinken and S. Lenaerts, *Appl. Catal., B*, 2011, **105**, 111–116.
30 M. Rashidimoghaddam, A. Saljooqi, T. Shamspur and A. Mostafavi, *New J. Chem.*, 2020, **44**, 15584–15592.
31 B. Yang, Z. Ma, Q. Li, X. Liu, Z. Liu, W. Yang, X. Guo and X. Jia, *New J. Chem.*, 2020, **44**, 1090–1096.
32 D. Carboni, L. Malfatti, A. Pinna, B. Lasio, Y. Tokudome, M. Takahashi and P. Innocenzi, *New J. Chem.*, 2013, **37**, 2995–3002.
33 Y. P. Bhoi, C. Behera, D. Majhi, S. M. Equeenuddin and B. G. Mishra, *New J. Chem.*, 2018, **42**, 281–292.
34 A. Aguera, E. Almansa, S. Malato, M. I. Maldonado and A. R. Fernandez-Alba, *Analusis*, 1998, **26**, 245–251.
35 C. Feng, G. Xu and X. Liu, *J. Rare Earths*, 2013, **31**, 44–48.
36 H. Liu, Y. Feng, J. Shao, Y. Chen, Z. L. Wang, H. Li, X. Chen and Z. Bian, *Nano Energy*, 2020, **70**, 104499.
37 J. Dong, J. Huang, A. Wang, G. V. Biesold-McGee, X. Zhang, S. Gao, S. Wang, Y. Lai and Z. Lin, *Nano Energy*, 2020, **71**, 104579.
38 S. Banerjee, D. D. Dionysiou and S. C. Pillai, *Appl. Catal., B*, 2015, **176**, 396–428.
39 W. Fa, L. Zan, C. Gong, J. Zhong and K. Deng, *Appl. Catal., B*, 2008, **79**, 216–223.
40 S. Cho and W. Choi, *J. Photochem. Photobiol., A*, 2001, **143**, 221–228.
41 M.-G. Jeong, E. J. Park, H. O. Seo, K.-D. Kim, Y. D. Kim and D. C. Lim, *Appl. Surf. Sci.*, 2013, **271**, 164–170.
42 E. I. Cedillo-González, C. Mugoni, M. Montorsi and C. Siligardi, *Appl. Surf. Sci.*, 2016, **378**, 73–79.
43 H. Einaga, S. Futamura and T. Ibusuki, *Appl. Catal., B*, 2002, **38**, 215–225.
44 W. Yuan, B. Zhu, X. Y. Li, T. W. Hansen and Y. J. S. Wang, *Science*, 2020, **367**, 428–430.
45 C. L. Pang, R. Lindsay and G. Thornton, *Chem. Rev.*, 2013, **113**, 3887–3948.
46 K. Onda, B. Li, J. Zhao, K. D. Jordan, J. L. Yang and H. Petek, *Science*, 2005, **308**, 1154–1158.
47 H. Hussain, G. Tocci, T. Woolcot, X. Torrelles, C. L. Pang, D. S. Humphrey, C. M. Yim, D. C. Grinter, G. Cabailh, O. Bikondoa, R. Lindsay, J. Zegenhagen, A. Michaelides and G. Thornton, *Nat. Mater.*, 2017, **16**, 461–466.
48 J. Balajka, U. Aschauer, S. F. L. Mertens, A. Selloni, M. Schmid and U. Diebold, *J. Phys. Chem. C*, 2017, **121**, 26424–26431.
49 W. Yuan, J. Meng, B. Zhu, Y. Gao, Z. Zhang, C. Sun and Y. Wang, *Chem. Mater.*, 2018, **30**, 288–295.
50 K. Shirai, G. Fazio, T. Sugimoto, D. Selli, L. Ferraro, K. Watanabe, M. Haruta, B. Ohtani, H. Kurata, C. Di Valentin and Y. Matsumoto, *J. Am. Chem. Soc.*, 2018, **140**, 1415–1422.
51 K. Shirai, T. Sugimoto, K. Watanabe, M. Haruta, H. Kurata and Y. Matsumoto, *Nano Lett.*, 2016, **16**, 1323–1327.
52 L. Ding, M. Li, Y. Zhao, H. Zhang, J. Shang, J. Zhong, H. Sheng, C. Chen and J. Zhao, *Appl. Catal., B*, 2020, **266**, 118634.
53 Y. Zhao, T. Shi, J. Shang, L. Ding, X. Cao, C. Chen and J. Zhao, *Appl. Catal., B*, 2020, **277**, 119234.
54 F. Han, Z. Zhou, Z. Huang, M. Li and L. Guo, *J. Phys. Chem. C*, 2018, **122**, 26965–26973.
55 C. Dette, M. A. Perez-Osorio, S. Mange, F. Giustino, S. J. Jung and K. Kern, *J. Phys. Chem. C*, 2018, **122**, 11954–11960.
56 Q. Wang, H. Zhu and B. Li, *Chem. Eng. J.*, 2019, **378**, 122072.
57 Q. Wang, L. Zhang, Y. Guo, M. Shen, M. Wang, B. Li and J. Shi, *Chem. Eng. J.*, 2020, **396**, 125347.
58 Y. Song, J. Jiang, Y. Ma, T. Li and S. Dong, *Catal. Sci. Technol.*, 2021, **11**, 2110–2118.
59 H. Lin, J. Long, Q. Gu, W. Zhang, R. Ruan, Z. Li and X. Wang, *Phys. Chem. Chem. Phys.*, 2012, **14**, 9468–9474.
60 C.-C. Chen, S.-H. Hu and Y.-P. Fu, *J. Alloys Compd.*, 2015, **632**, 326–334.
61 G. Kresse and J. J. P. R. B. Furthmüller, *Phys. Rev. B: Condens. Matter Mater. Phys.*, 1996, **54**, 11169–11186.
62 G. Kresse and D. J. P. R. B. Joubert, *Phys. Rev. B: Condens. Matter Mater. Phys.*, 1999, **59**, 1758–1775.
63 S. Nosé, *J. Chem. Phys.*, 1984, **81**, 511–519.
64 S. Grimme, J. Antony, S. Ehrlich and H. Krieg, *J. Chem. Phys.*, 2010, **132**, 105113.
65 M. Bourgin, F. Violleau, L. Debrauwer and J. Albet, *J. Hazard. Mater.*, 2011, **190**, 60–68.
66 X. L. Cui, X. T. Liu, C. Y. Lin, M. C. He and W. Ouyang, *Chemosphere*, 2020, **254**, 12.
67 S. Liu, Z. Zheng, F. Wei, Y. Ren, W. Gui, H. Wu and G. Zhu, *J. Agric. Food Chem.*, 2010, **58**, 3271–3278.
68 C. Blasco, M. Fernández, Y. Picó, G. Font and J. Maes, *Anal. Chim. Acta*, 2002, **461**, 109–116.
69 B. K. Lavine, T. Ding and D. Jacobs, *Anal. Lett.*, 2010, **43**, 1812–1821.
70 Q. Wang, C. Fan, G. Li, J. Luo and B. Li, *Catal. Sci. Technol.*, 2019, **9**, 7023–7033.
71 Q. Wang, S. Guan and B. Li, *Catal. Sci. Technol.*, 2017, **7**, 4064–4078.
72 M. Gong, Y. Li, Y. Guo, X. Lv and X. Dou, *Sens. Actuators, B*, 2018, **262**, 350–358.